View metadata, citation and similar papers at core.ac.uk

brought to you by CORE

provided by Edinburgh Research Explorer

THE UNIVERSITY of EDINBURGH

Edinburgh Research Explorer

Phase transition boundary between fcc and hcp structures in Fe-Si alloy and its implications for terrestrial planetary cores

Citation for published version:
Komabayashi, T, Pesce, G, Morard, G, Antonangeli, D, Sinmyo, R & Mezouar, M 2019, 'Phase transition boundary between fcc and hcp structures in Fe-Si alloy and its implications for terrestrial planetary cores', *American Mineralogist*, vol. 104, no. 1, pp. 94-99. https://doi.org/10.2138/am-2019-6636

Digital Object Identifier (DOI):
10.2138/am-2019-6636

Link:
Link to publication record in Edinburgh Research Explorer

Document Version:
Peer reviewed version

Published In:
American Mineralogist

General rights
Copyright for the publications made accessible via the Edinburgh Research Explorer is retained by the author(s) and / or other copyright owners and it is a condition of accessing these publications that users recognise and abide by the legal requirements associated with these rights.

Take down policy
The University of Edinburgh has made every reasonable effort to ensure that Edinburgh Research Explorer content complies with UK legislation. If you believe that the public display of this file breaches copyright please contact openaccess@ed.ac.uk providing details, and we will remove access to the work immediately and investigate your claim.

Download date: 12. Jan. 2020

Revision 2

Phase transition boundary between fcc and hcp structures in Fe-Si alloy and its implications for terrestrial planetary cores

Tetsuya Komabayashi[1*], Giacomo Pesce[1], Guillaume Morard[2], Daniele Antonangeli[2], Ryosuke Sinmyo[3†], Mohamed Mezouar[4]

[1]School of GeoSciences and Centre for Science at Extreme Conditions, University of Edinburgh EH9 3FE, UK

[2]Sorbonne Université, Muséum National d'Histoire Naturelle, UMR CNRS 7590, IRD, Institut de Minéralogie, de Physique des Matériaux et de Cosmochimie, IMPMC, 75005 Paris, France

[3]Bayerisches Geoinstitut, Universitat Bayreuth, 95440 Bayreuth, Germany

[4]European Synchrotron Radiation Facility, BP 220, F-38043 Grenoble Cedex, France

*corresponding author: Tetsuya Komabayashi
E-mail: tetsuya.komabayashi@ed.ac.uk

[†]Now at Department of Earth and Planetary Science, University of Tokyo, 7-3-1 Hongo, Bunkyo, Tokyo 113-0033, Japan

ABSTRACT

The phase transition between a face-centered cubic (fcc) and hexagonal close-packed (hcp) structures in Fe-4wt% Si alloy was examined in an internally resistive heated diamond anvil cell (DAC) under high-pressure (*P*) and -temperature (*T*) conditions to 71 GPa and 2000 K by *in-situ* synchrotron X-ray diffraction. Complementary laser-heated DAC experiments were performed in Fe-6.5wt% Si. The fcc-hcp phase transition boundaries in the Fe-Si alloys are located at higher temperatures than that in pure Fe, indicating that the addition of Si expands the hcp stability field. The dP/dT slope of the boundary of the entrant fcc phase in Fe-4wt% Si is similar to that of pure Fe, but the two-phases region is observed over a temperature range increasing with pressure, going from 50 K at 15 GPa to 150 K at 40 GPa. The triple point, where the fcc, hcp, and liquid phases coexist in Fe-4wt% Si, is placed at 90-105 GPa and 3300-3600 K with the melting curve same as in Fe is assumed. This supports the idea that the hcp phase is stable at Earth's inner core conditions. The stable structures of the inner cores of the other terrestrial planets are also discussed based on their P-T conditions relative to the triple point. In view of the reduced P-T conditions of the core of Mercury (well below the triple point), an Fe-Si alloy with a Si content up to 6.5 wt% would likely crystallize an inner core with an fcc structure. Both Venusian and Martian cores are believed to

currently be totally molten. Upon secular cooling, Venus is expected to crystallize an inner core with an hcp structure, as the pressures are similar to those of the Earth's core (far beyond the triple point). Martian inner core will take an hcp or fcc structure depending on the actual Si content and temperature.

Key words

Earth's core; high-pressure; diamond anvil cell; internal resistive heating; Fe-Si alloy

INTRODUCTION

Terrestrial core formation process has been discussed in relation to metal-silicate equilibration during accretion stage (Li and Agee 1996; Wade and Wood 2005; Siebert et al. 2013) although some recent models considered disequilibrium processes at a later stage (Rubie et al. 2011). The metal-silicate equilibration inevitably results in an impure iron rich metallic core (Wade and Wood; Siebert et al. 2013). The impurity includes nickel and several less dense elements which are also called light elements (Poirier 1994; Allègre et al. 1995).

Birch (1952) pointed out that the density of pure iron might be greater than the seismological determination for Earth's core. Such a density deficit has been associated

37 with the presence of lighter element(s), and a recent internally consistent
38 thermodynamic model of pure iron estimated the core density deficit to be 7% for the
39 outer core and 4.5 % for the inner core (Komabayashi 2014). Other terrestrial planetary
40 cores also likely contain light elements considering metal-silicate partitioning during
41 their cores formation. In addition, the presence of a magnetic field found in some
42 terrestrial planets may indicate the presence of a light element-bearing partially molten
43 core (e.g., Sohl and Schubert 2007). Light elements would be expelled at the bottom of
44 the liquid outer core as it is less partitioned in the solid inner core and this would drive
45 convection in the outer core (Stevenson et al. 1983; Lister and Buffett 1995).

46 Among the potential light elements, silicon is considered a plausible candidate
47 for the terrestrial planetary cores for various reasons: i) silicon is the second most
48 abundant element in the mantle and series of high-pressure (P) and –temperature (T)
49 experiments demonstrated that silicon and oxygen could be dissolved from mantle
50 silicates to core melt (Takafuji et al. 2005; Ozawa et al. 2009), and then silicon is
51 partitioned between solid and liquid during core crystallization; ii) silicon isotopic
52 composition of stony meteorites is different from bulk silicate Earth (Georg et al. 2007;
53 Fitoussi et al. 2009), implying that silicon might have been partitioned into the core
54 during core-mantle differentiation (Shahar et al. 2011; Hin et al. 2014); iii) all the core

55 formation models based on silicate-metal equilibration inevitably have silicon as a light
56 element in the core (Wade and Wood 2005; Rubie et al. 2011; Siebert et al. 2013).

57 Phase relations and equations of state (EoS) of solid phases in the system
58 Fe-(Fe)Si have been extensively studied by both experiment and theory (Alfe et al.
59 2002; Dobson et al. 2002; Lin et al. 2002; Kuwayama and Hirose 2004; Lin et al. 2009;
60 Tateno et al. 2015; Ozawa et al. 2016). An important phase relation is the transition
61 between face-centered cubic (fcc) and hexagonal close-packed (hcp) structures, as this
62 is central to address the solid inner core structure (Uchida et al. 2001; Asanuma et al.
63 2008; Komabayashi et al. 2009), and the P-T location of the phase boundary can be
64 used to deduce thermodynamic properties (Wood 1993; Komabayashi 2014). Notably,
65 the triple point P-T location where the hcp, fcc, and liquid phases coexist can be
66 constrained from the fcc-hcp boundary and melting curve (Zhang et al. 2016). An
67 experimental study in a laser-heated diamond anvil cell (DAC) reported that the
68 transition temperature was greatly reduced when 3.4 wt%Si was added to Fe (Asanuma
69 et al. 2008). In contrast, phase relations inferred by Fischer et al. (2013) suggested that
70 addition of silicon should increase the transition temperature. Tateno et al. (2015)
71 experimentally demonstrated that the transition temperature was increased by the
72 addition of 6.5 wt%Si to iron. As such the effect of Si on the transition temperature has

been a controversy and the P-T conditions of the actual boundaries in the system Fe-Si are not unanimous.

In this study, we present the investigation of the P-T locations of the fcc-hcp transition boundaries in Fe-Si alloys in an internally resistive heated DAC. The internally heated DAC heats the sample by its resistance, with an improved accuracy in temperature with respect to conventional laser heated DAC (Komabayashi et al. 2009; 2012). Based on these experimental results, we will discuss the effect of Si on the Fe properties under high P-T condition and address the stable structure of a solid Fe-Si alloy at the conditions of the inner cores of the terrestrial planets of the solar system.

EXPERIMENTAL PROCEDURE

We conducted high-P-T in-situ X-ray diffraction (XRD) experiments on Fe-Si samples at the beamline ID27, European Synchrotron Radiation Facility (ESRF). X-rays with a wavelength of 0.3738Å were focused to a 3x3 μm^2 spot at sample position and the diffracted X-rays were collected on a two dimensional detector (mar345 Image Plate Detector). The collection time was 10 seconds for each measurement. Using the fit-2D program (Hammersley 1996), the obtained data were converted to the conventional one-dimensional XRD pattern.

High pressure was generated in a DAC with a pair of diamond anvils with a culet size of 300 μm or 150-450 μm beveled depending on the pressure range. The starting material was a 5-7 μm thick Fe-Si alloy with 4 wt% Si (Rare Metallic. Co., hereafter Fe-4Si), placed in the sample chamber and connected to platinum leads. The junction between the Fe sample and Pt leads was outside the sample chamber (see Komabayashi et al. (2009) for the sample geometry). SiO_2 glass layers served as a pressure transmitting medium and thermal insulator. High temperature was achieved with an internal resistive system (Komabayashi et al. 2009; 2012; Antonangeli et al. 2012). The sample was resistively heated by directly applying a DC voltage by an external power supply. The temperature was measured by a spectral radiometric system as conventional in laser heating experiments. Noteworthy, thanks to the improved time and spatial stability of the hotspot and the reduced thermal gradients, resulting uncertainties in temperature were about 50 K (Komabayashi et al., 2012)

Complementary laser heating experiments were conducted on an Fe-6.5Si sample (Rare Metallic. Co.) at ID27, ESRF (see Morard et al. (2011) for details of the laser heating experimental set up). The internal heating system was not applied because this alloy is so brittle that it was not possible to make it into thin foil. Irrespectively of the use of low numerical aperture and reflecting objectives which effectively minimize

the chromatic aberration and improve reliability of temperature determination (Mezouar et al. 2017), the laser heating experiments show larger temperature uncertainty due to large temperature gradient across the sample and laser fluctuations. The two microns diameter pinhole at the entrance of the spectrometer allows for a collection of signal only coming from the very central part of the hotspot and an optimal alignment of lasers and X-ray beam. Morard et al. (2011) discussed that the possible uncertainty in the temperature in this experimental setup might be 150 K at 3000 K. In the present study, we assumed a more conservative number, 10% of the generated temperature.

In all the runs, the pressure at any given temperature was calculated with a thermal EoS for Fe-4Si or Fe-6.5Si with the hcp structure that was assessed based on pure iron (Dewaele et al. 2006) and Fe-9wt%Si (Tateno et al. 2015). The room temperature parameters for the Vinet EoS were obtained by averaging on the basis of mole fraction between the two compositions: for Fe-4Si, V_0 = 22.56Å^3, K_0 = 166 GPa, K' = 5.4, and for Fe-6.5Si, V_0 = 22.63 Å^3, K_0 = 167 GPa, K' = 5.5, where V_0, K_0, K' are the unit-cell volume, bulk modulus, and its pressure derivative at 300 K and 1 bar, respectively. We assumed the same thermal parameters as for pure iron (Dewaele et al. 2006; Tateno et al. 2015).

The thermal pressure effect on the sample pressure was checked against the

127 pressure for the SiO_2 pressure medium. The EoS for stishovite by Wang et al (2012) was
128 used to calculate the pressure for SiO_2. As the precise temperature for the pressure
129 medium was unknown, we calculated the pressure for SiO_2 at the sample temperature
130 and 300 K. At 42.8 GPa and 1940 K for the sample, the pressure for SiO_2 were 44.9
131 GPa and 34.1 GPa at 1940 K and 300 K respectively. Since the crystallized portion of
132 the pressure medium should be at the same (or slightly lower) temperature of the sample,
133 the above calculation independently supports our pressure determination for the iron
134 alloy. Also, after quench, the pressure for SiO_2 is 37.6 ± 1.0 GPa, which is consistent
135 with the sample pressure of 36.6 ± 0.4 GPa. Therefore, we can conclude that the
136 pressure estimation at high temperatures is reasonable.
137 The use of the unit-cell volume of the hcp phase in the pressure calculation
138 may introduce an uncertainty when the experimental condition is near the completion of
139 the hcp-fcc reaction. Based on a binary temperature-composition (T-X) phase loop
140 detailed below, the pressure could have been underestimated by less than 1.3 GPa at 40
141 GPa and 1870K. When the unit-cell volume for the hcp phase was not obtained, due to
142 either grain growth or complete transition to the fcc phase, we assumed constant
143 pressure upon further heating.
144

RESULTS

Fe-4Si

Six separate in-situ XRD experiments were carried out on the Fe-4Si sample in the internally heated DAC. The results are illustrated in Fig. 1a and summarized in Table 1.

In the first run, the sample was compressed to 16.4 GPa and the XRD pattern shows coexistence of the bcc and hcp phases. Then the sample was heated to 1060 K and the fcc phase, with a minor amount of hcp phase, was observed. The hcp phase disappeared in the following XRD pattern at a similar temperature of 1050 K. Temperature slightly increased with time to 1080 K at steady power from the DC power supply without further changes in the pattern. Then, we tried to reverse the reaction. As the spectroradiometric method could not reliably measure temperatures below 1000 K, the temperature was estimated based on the linear power-temperature relationship established at 1060 K. During the cooling path, the reversal reaction started at 860 K, 200 K lower than the reaction in the forward heating cycle. Further decreasing temperature to 770 K only slightly promoted the reaction, which suggests that nucleation of the hcp phase is very sluggish and implies that the width of the reaction in the backward cycle is much wider than the forward cycle. Accordingly, we constrained

the P-T conditions of the reaction in the forward cycle only and the results of the backward cycle are not listed in Table 1 to avoid confusion.

In the following runs, we only employed heating cycles which started from the hcp phase towards the fcc stability field. In the runs 2, 3, and 4, we observed a transition sequence from hcp to hcp+fcc and to fcc with increasing temperature. Figure 2 shows a series of XRD patterns collected during the run 2 for increasing temperature at about 24 GPa. The temperature was first held at 1120 K for 4 minutes, observing only the hcp phase. Then we increased the temperature to 1230 K and fcc peaks appeared. No further changes in the XRD pattern were recognized during the following 40 minutes, during which the temperature was kept constant. We further increased the temperature to 1260 K, which instantaneously increased the intensity of the fcc peaks. During the following 30 minutes at constant temperature, the XRD patterns did not show significant changes. The transition was completed at 1330 K. In summary, the drastic changes in XRD were observed only upon temperature increase. The transition from the hcp to fcc phase seems to be very fast, with minimal kinetic effects.

In the runs 5 and 6, we observed no structural change to the highest temperatures and confirmed stability of the hcp phase to 71.0 GPa and 2020 K.

Overall, thanks to the performances of the internal heating system, we have

been able to place tight constraints on the P-T location of the transition boundaries. In particular, the width of the phase loop was accurately constrained. The dP/dT slope of the boundary of the entrant fcc phase in Fe-4wt% Si is similar to that of pure Fe, while the temperature interval of the two-phase region expands with increasing pressure from 50 K at 15 GPa to 150 K at 40 GPa (Fig. 1a).

Fe-6.5Si

Two separate laser-heating runs were conducted on the Fe-6.5Si sample (Fig. 1b). Same as for the internal-heating runs, we increased the temperature under high pressures. In the first run, we compressed the sample to 24.0 GPa at room temperature and then heated it by laser, reporting the appearance of fcc peaks at 1850 K in coexistence with hcp peaks. In the second run, we observed a complete transition to the fcc phase at 2340 K and 56.6 GPa. Considering the uncertainty in temperature in the laser heating experiment (i.e., ±10%), the present experimental data are consistent with results by Tateno et al. (2015) (Fig. 1b).

DISCUSSION

Effect of Si on the fcc-hcp transition

The present experiments confirmed the enlarged high temperature stability of the hcp phase in Fe-4Si and Fe-6.5Si with respect to the case in pure Fe (Fig. 1), in agreement with Fischer et al. (2013) and Tateno et al. (2015) but in contrast to Asanuma et al. (2008). Dissecting the XRD patterns in Asanuma et al. (2008), we noted that they assigned tiny shallow rises as peaks from the fcc phase, while the appearance of the fcc phase is clearly marked by the presence of the (200) peak (Fig. 2) (Komabayashi et al. 2009; 2012). We conclude that the transition temperature between the hcp and fcc phases increases with Si content.

Figure 3 shows a T-X diagram at 40 GPa based on the present data on Fe-4Si and Fe-6.5Si and existing experimental data on pure Fe and Fe-9Si (Komabayashi et al. 2009; Tateno et al. 2015). The fcc-hcp transition temperature increases with Si content. The P-T conditions for a reaction hcp = hcp + B2 phase (Tateno et al. 2015) placed additional constraint on the phase diagram (Fig. 3). The maximum solubility of Si into the fcc phase should be about 7 wt%. A thermodynamic model will be made to fit the data in the near future.

IMPLICATIONS

Figure 4 shows a phase diagram of iron alloys reporting the fcc-hcp boundaries

217 in Fe, Fe-4Si, and Fe-6.5Si, together with the P-T ranges for the cores of Mars and
218 Mercury. Addition of Si to Fe expands the stability of the hcp phase as confirmed by the
219 P-T locations of the fcc-hcp transitions observed in this study, which are consistent with
220 Tateno et al. (2015) based on a laser-heated DAC experiments (Fig. 1b). The triple point
221 where the fcc, hcp, and liquid phases coexist in Fe-4wt% Si is placed at 90-105 GPa and
222 3300-3600 K (the melting curve is assumed to be the same as in Fe as Si inclusion at
223 4wt% level should not significantly affect the melting temperature (Morard et al. 2011)),
224 supporting the idea that Earth's inner core at 330-364 GPa is made up with the hcp
225 phase. Tateno et al. (2015) similarly proposed that the inner core would be made of a
226 sole hcp alloy if the Si content is up to 7 wt.%.

227 More complex can be the cases for the other terrestrial planets of the solar
228 system, namely, Venus, Mercury, and Mars. Due to the lack of seismic data,
229 information about their internal structures heavily depends on the average density. As
230 such, the core density deficit cannot be pertinently discussed. Nevertheless geophysical
231 modelling studies argued for the presence of light elements in the cores and kept this
232 into consideration when simulating planetary core, and in particular when discussing
233 their molten/solid state (Stevenson et al. 1983; Williams and Nimmo 2004; Rivoldini et
234 al. 2011; Dumberry and Rivoldini 2015; Knibbe and van Westrenen 2018). In the

following, we will limit our discussion to the Fe-Si-S system. Tsujino et al. (2013) summarized existing thermal models for terrestrial core-mantle boundaries in the system Fe-S (Stevenson et al. 1983; Sohl and Spohn 1997; Fei et al. 2000; Williams and Nimmo 2004) and assessed the adiabats across the cores on the basis of the Grüneisen parameter for pure fcc iron (Fig. 4). The known reduction of the crystallizing temperature of iron by addition of silicon (Kubaschewski 1993; Kuwayama and Hirose 2004) implies that the thermal profiles in Fig. 4, which are based on the liquidus of the system Fe-S, can be considered as the maximum estimates for the system Fe-Si-S.

Venus' similar size to the Earth implies that its internal structure is differentiated into crust, mantle, and core (Sohl and Schubert 2007). However, contrarily to the Earth, Venus does not have a global magnetic field .The pressure at the center of the planet was estimated to be 295 GPa which is slightly lower than of the Earth and crystallization of the liquid core might have not yet started (Stevenson et al. 1983). Since the core pressure is far greater than the triple point pressure in the system Fe-4Si (Fig. 4), when upon secular cooling the inner core will start crystallizing, likewise the Earth, it should take an hcp phase.

It is suggested that Mercury has a partially molten iron core as it shows a dipole magnetic field from a spacecraft observation (Ness 1979). Further support of the

253 presence of a liquid portion of the core comes from and the amplitude of its librations
254 (Margot et al. 2005). The suggested thermal structure of Mercurian core modeled on the
255 basis of the system Fe-S argues for a temperature much higher than the fcc-hcp
256 transition in Fe-6.5Si (Fig. 4). Recently proposed thermal models of Fe-Si cores showed
257 a similar temperature range as in Fig. 4 (Knibbe and van Westrenen 2018). Hence
258 Mercurian inner core is expected to take an fcc structure if the Si content is less than 6.5
259 wt%. Only upon further cooling, the fcc-structured alloy in Mercurian inner core, will
260 be transformed to the hcp phase.

261 Mars currently does not have an active global magnetic field, although it has a
262 metallic core in view of its average density and moment of inertia (Yoder et al. 2003).
263 However, the presence of magnetized rock records found in southern highland area
264 indicates that the planet should have had a magnetic field in the past. Stevenson et al.
265 (1983) suggested that present Martian core should still be totally molten to account for
266 the absence of the magnetic field and the rocks were magnetized by a field produced by
267 a past, now extinct, thermal convection of the liquid core. The inferred thermal profiles
268 of the core partially overlap with the fcc-hcp transition in Fe-4Si (Fig. 4). As such the
269 first iron alloy crystal that will crystallize in the future will be either fcc or hcp phase
270 depending on the actual Si content and exact temperature. In the case of the fcc phase, it

will be transformed to the hcp phase as the core further cools down.

In summary, the inner core structure of the terrestrial planets can be discussed based on the phase relations in Fig. 4. The hcp core would show more anisotropic seismic properties (Steinle-Neumann et al., 2001) than the fcc core because of the anisotropic crystal structure. Also the hcp core would be denser than the fcc core as the fcc-hcp transition in Fe-4Si shows about 0.8% density jump. Those changes are important in future attempts to construct a precise density model for the planetary interior.

Acknowledgements

The synchrotron experiments were performed at ID27 ESRF. This research was supported by the European Research Council (ERC) Consolidator Grant to TK (Earth core #647723).

References

Alfè, D., Gillan, M.J., and Price, G.D. (2002) Composition and temperature of the Earth's core constrained by combining ab initio calculations and seismic data. Earth and Planetary Science Letters 195, 91-98.

Allègre, C.J., Poirier, J.P., Humler, E., and Hofmann, A.W. (1995) The chemical composition of the Earth. Earth and Planetary Science Letters 134, 515-526.

Anderson, J.D., Colombo, G., Esposito, P.B., Lau, E.L., and Trager, G.B. (1987) The Mass, Gravity-Field, and Ephemeris of Mercury. Icarus 71, 337-349.

Antonangeli, D., Komabayashi, T., Occelli, F., Borissenko, E., Walters, A.C., Fiquet, G., and Fei, Y.W. (2012) Simultaneous sound velocity and density measurements of hcp iron up to 93 GPa and 1100 K: An experimental test of the Birch's law at high temperature. Earth and Planetary Science Letters 331, 210-214.

Asanuma, H., Ohtani, E., Sakai, T., Terasaki, H., Kamada, S., Hirao, N., Sata, N., and Ohishi, Y. (2008) Phase relations of Fe-Si alloy up to core conditions: Implications for the Earth inner core. Geophysical Research Letters 35, L12307, doi:10.1029/2008GL033863.

Birch, F. (1952) Elasticity and constitution of the Earth's interior. Journal of Geophysical Research 57, 227-286.

304 Dewaele, A., Loubeyre, P., Occelli, F., Mezouar, M., Dorogokupets, P.I., and Torrent, M.
305 (2006) Quasihydrostatic equation of state of iron above2 Mbar. Physical Review
306 Letters 97, 215504.
307 Dobson, D.P., Vocadlo, L., and Wood, I.G. (2002) A new high-pressure phase of FeSi.
308 American Mineralogist 87, 784-787.
309 Dumbarry, M., Rivoldini, A. (2015) Mercury's inner core size and core-crystallization
310 regime. Icarus 248, 254–268.
311 Fei, Y.W., Li, J., Bertka, C.M., and Prewitt, C.T. (2000) Structure type and bulk
312 modulus of Fe3S, a new iron-sulfur compound. American Mineralogist 85,
313 1830-1833.
314 Fischer, R.A., Campbell, A.J., Reaman, D.M., Miller, N.A., Heinz, D.L., Dera, P., and
315 Prakapenka, V.B. (2013) Phase relations in the Fe-FeSi system at high pressures
316 and temperatures. Earth and Planetary Science Letters 373, 54-64.
317 Fitoussi, C., Bourdon, B., Kleine, T., Oberli, F., and Reynolds, B.C. (2009) Si isotope
318 systematics of meteorites and terrestrial peridotites: implications for Mg/Si
319 fractionation in the solar nebula and for Si in the Earth's core. Earth and
320 Planetary Science Letters 287, 77-85.
321 Georg, R.B., Halliday, A.N., Schauble, E.A., and Reynolds, B.C. (2007) Silicon in the

322 Earth's core. Nature 447, 1102-1106, doi:10.1038/nature05927.
323 Hammersley, J. (1996) *FIT2D V12.012 Reference Manual*. Eur. Synchrotron Radiat.
324 Facil., Grenoble, France.
325 Hin, R.C., Fitoussi, C., Schmidt, M.W., and Bourdon, B. (2014) Experimental
326 determination of the Si isotope fractionation factor between liquid metal and
327 liquid silicate. Earth and Planetary Science Letters 387, 55-66.
328 Knibbe, J.S., and van Westrenen, W. (2018) The thermal evolution of Mercury's Fe-Si
329 core. Earth and Planetary Science Letters 482, 147-159.
330 Komabayashi, T. (2014) Thermodynamics of melting relations in the system Fe-FeO at
331 high pressure: Implications for oxygen in the Earth's core. Journal of
332 Geophysical Research 119, DOI: 10.1002/2014JB010980.
333 Komabayashi, T., Fei, Y., Meng, Y., and Prakapenka, V. (2009) In-situ X-ray diffraction
334 measurements of the γ-ε transition boundary of iron in an internally-heated
335 diamond anvil cell. Earth and Planetary Science Letters 282, 252-257.
336 Komabayashi, T., Hirose, K., and Ohishi, Y. (2012) In situ X-ray diffraction
337 measurements of the fcc-hcp phase transition boundary of an Fe-Ni alloy in an
338 internally heated diamond anvil cell. Physics and Chemistry of Minerals 39,
339 329-338.

340 Kubaschewski, O. (1993) in: Okamoto, H. (Ed.), Phase diagram of binary iron alloys.
341 ASM International, Ohio, p. 380.
342 Kuwayama, Y., and Hirose, K. (2004) Phase relations in the system Fe-FeSi at 21 GPa.
343 American Mineralogist 89, 273-276.
344 Li, J., and Agee, C.B. (1996) Geochemistry of mantle-core differentiation at high
345 pressure. Nature 381, 686-689.
346 Lin, J.F., Heinz, D.L., Campbell, A.J., Devine, J.M., and Shen, G.Y. (2002) Iron-silicon
347 alloy in Earth's core? Science 295, 313-315.
348 Lin, J.F., Scott, H.P., Fischer, R.A., Chang, Y.Y., Kantor, I., and Prakapenka, V.B. (2009)
349 Phase relations of Fe-Si alloy in Earth's core. Geophysical Research Letters 36,
350 L06306, doi:10.1029/2008GL036990.
351 Lister, J.R., and Buffett, B.A. (1995) The Strength and Efficiency of Thermal and
352 Compositional Convection in the Geodynamo. Physics of the Earth and
353 Planetary Interiors 91, 17-30.
354 Margot, J. L., Peale, S. J., Jurgens, R. F., Slade, M. A., and Holin, I. V. (2007) Large
355 Longitude Libration of Mercury Reveals a Molten Core. Science 316, 710-714.
356 Mezouar, M., Giampaoli, R., Garbarino, G., Kantor, I., Dewaele, A., Weck, G., Boccato,
357 S., Svitlyk, V., Rosa, A.D., Torchio, R., Mathon, O., Hignette, O., and Bauchau,

358 S. (2017) Methodology for in situ synchrotron X-ray studies in the laser-heated
359 diamond anvil cell. High Pressure Research 37, 170-180.
360 Morard, G., Andrault, D., Guignot, N., Siebert, J., Garbarino, G., and Antonangeli, D.
361 (2011) Melting of Fe-Ni-Si and Fe-Ni-S alloys at megabar pressures:
362 implications for the core-mantle boundary temperature. Physics and Chemistry
363 of Minerals 38, 767-776.
364 Ness, N.F. (1979) Magnetic-Fields of Mercury, Mars, and Moon. Annual Review of
365 Earth and Planetary Sciences 7, 249-288.
366 Ozawa, H., Hirose, K., Mitome, M., Bando, Y., Sata, N., and Ohishi, Y. (2009)
367 Experimental study of reaction between perovskite and molten iron to 146 GPa
368 and implications for chemically distinct buoyant layer at the top of the core.
369 Physics and Chemistry of Minerals 36, 355-363.
370 Ozawa, H., Hirose, K., Yonemitsu, K., and Ohishi, Y. (2016) High-pressure melting
371 experiments on Fe-Si alloys and implications for silicon as a light element in the
372 core. Earth and Planetary Science Letters 456, 47-54.
373 Rivoldini, A., Van Hoolst, Verhoeven, O., Mocquet, A., Dehant V. (2011) Geodesy
374 constraints on the interior structure and composition of Mars. Icarus 213, 451–
375 472.

376 Rubie, D.C., Frost, D.J., Mann, U., Asahara, Y., Nimmo, F., Tsuno, K., Kegler, P.,
377 Holzheid, A., and Palme, H. (2011) Heterogeneous accretion, composition and
378 core-mantle differentiation of the Earth. Earth and Planetary Science Letters 301,
379 31-42.
380 Shahar, A., Hillgren, V.J., Young, E.D., Fei, Y.W., Macris, C.A., and Deng, L.W. (2011)
381 High-temperature Si isotope fractionation between iron metal and silicate.
382 Geochimica et Cosmochimica Acta 75, 7688-7697.
383 Siebert, J., Badro, J., Antonangeli, D., and Ryerson, F.J. (2013) Terrestrial Accretion
384 Under Oxidizing Conditions. Science 339, 1194-1197.
385 Sohl, F., and Schubert, G. (2007) Interior structure, composition, and mineralogy of the
386 terrestrial planets, in: Schubert, G. (Ed.), Treatise on Geophysics, pp. 27-68.
387 Sohl, F., and Spohn, T. (1997) The interior structure of Mars: Implications from SNC
388 meteorites. Journal of Geophysical Research-Planets 102, 1613-1635.
389 Steinle-Neumann, G., Stixrude, L., Cohen, R.E., and Gülseren, O. (2001) Elasticity of
390 iron at the tempeature of the Earth's inner core. Nature 413, 57-60.
391 Stevenson, D.J., Spohn, T., and Schubert, G. (1983) Magnetism and Thermal Evolution
392 of the Terrestrial Planets. Icarus 54, 466-489.
393 Takafuji, N., Hirose, K., Mitome, M., and Bando, Y. (2005) Solubilities of O and Si in

liquid iron in equilibrium with (Mg,Fe)SiO_3 perovskite and the light elements in the core. Geophysical Research Letters 32, L06313, doi:10.1029/2005GL022773.

Tateno, S., Kuwayama, Y., Hirose, K., and Ohishi, Y. (2015) The structure of Fe-Si alloy in Earth's inner core. Earth and Planetary Science Letters 418, 11-19.

Tsujino, N., Nishihara, Y., Nakajima, Y., Takahashi, E., Funakoshi, K., and Higo, Y. (2013) Equation of state of gamma-Fe: Reference density for planetary cores. Earth and Planetary Science Letters 375, 244-253.

Uchida, T., Wang, Y., Rivers, M.L., and Sutton, S.R. (2001) Stability field and thermal equation of state of ε-iron determined by synchrotron X-ray diffraction in a multianvil apparatus. Journal of Geophysical Research 106, 21709-21810.

Wade, J., and Wood, B.J. (2005) Core formation and the oxidation state of the Earth. Earth and Planetary Science Letters 236, 78-95.

Wang, F.L., Tange, Y., Irifune, T., and Funakoshi, K. (2012) P-V-T equation of state of stishovite up to mid-lower mantle conditions. Journal of Geophysical Research-Solid Earth 117, B06209, doi:10.1029/2011JB009100.

Williams, J.P., and Nimmo, F. (2004) Thermal evolution of the Martian core: Implications for an early dynamo. Geology 32, 97-100.

412 Wood, B.J. (1993) Carbon in the core. Earth and Planetary Science Letters 117,
413 593-607.
414 Yoder, C.F., Konopliv, A.S., Yuan, D.N., Standish, E.M., and Folkner, W.M. (2003)
415 Fluid core size of mars from detection of the solar tide. Science 300, 299-303.
416 Zhang, D.Z., Jackson, J.M., Zhao, J.Y., Sturhahn, W., Alp, E.E., Hu, M.Y., Toellner, T.S.,
417 Murphy, C.A., and Prakapenka, V.B. (2016) Temperature of Earth's core
418 constrained from melting of Fe and Fe0.9Ni0.1 at high pressures. Earth and
419 Planetary Science Letters 447, 72-83.
420

421 Figure captions

422

423 Figure 1. Results of the experiments in (a) Fe-4Si and (b) Fe-6.5Si. The phases observed
424 in XRD patterns are plotted: inversed triangle, hcp+bcc; square, hcp; normal triangle,
425 fcc+hcp; circle, fcc. In (a), the boundaries between the fcc and hcp phases in pure iron
426 (Komabayashi et al. 2009) and Fe-3.4Si (Asanuma et al. 2008) are also plotted. The data
427 with asterisk have larger temperature uncertainty. In (b), our data are shown together
428 with experimental data by Tateno et al. (2015). The typical uncertainty (2.5 GPa and
429 200 K) is shown for a guide to the eye, see Table 1 for the uncertainty for each data
430 point. The two datasets are fairly consistent considering the uncertainty in the laser
431 heating experiments.

432

433 Figure 2. Series of XRD patterns collected in the run 2 for increasing temperature. The
434 presence of the fcc phase was unambiguously marked by the appearance of (200) peak.

435

436 Figure 3. Temperature-composition diagram for the fcc-hcp transition. The open circle
437 denotes the transition temperature in pure Fe (Komabayashi et al. 2009); the star
438 symbols are the fcc-hcp reactions constrained by the present experiments; the filled
439 circle is the P-T condition for a reaction of hcp = hcp + B2 phase observed in Tateno et

440 al. (2015). The stability fields of fcc+B2 and hcp+B2 were constrained by phase
441 relations. In particular: (i) the boundary hcp = hcp+B2 should have a negative slope
442 (Tateno et al. 2015) and (ii) the invariant boundary where the fcc, hcp, and B2 phases
443 coexist should be placed at a temperature higher than the upper star at Fe-6.5Si.
444
445 Figure 4. The fcc-hcp boundaries in Fe-4Si and Fe-6.5Si (this study) with phase
446 relations of pure iron (black lines) (Komabayashi et al. 2009; Komabayashi 2014).
447 Thermal profiles of Mercurian and Martian cores in the system Fe-S are also shown
448 (Tsujino et al. 2013).

Table 1. Experimental conditions and results

Run	P, GPa	T, K*	Phase	V(hcp), Å^3	a (hcp), Å	c (hcp), Å	V(fcc), Å^3	Remarks
Fe-4Si (internal resistive heating)								
1	16.4(6)	300	bcc+hcp	20.823(53)	2.4640(18)	3.9604(83)		
	13.1(4)	1060	fcc+hcp(small)	21.660(0)	2.4855(0)	4.04853(0)	43.643(14)	
	13.1(4)	1050	fcc				43.615(19)	
	13.1(4)	1080	fcc				43.683(19)	
2	23.6(4)	300	hcp	20.265(27)	2.4394(14)	3.9323(24)		
	22.6(4)	1120	hcp	20.816(3)	2.4554(2)	3.9866(3)		
	21.9(5)	1230	hcp+fcc	20.955(3)	2.4596(2)	3.9998(3)	42.352(0)	
	21.2(4)	1260	hcp+fcc	21.036(0)	2.4596(0)	4.0152(0)	42.343(38)	
	21.2	1260	hcp+fcc	-	-	-	42.330(5)	one peak for hcp
	21.2	1270	hcp+fcc	-	-	-	42.370(4)	one peak for hcp
	21.2	1330	fcc				42.475(15)	
	21.2	1360	fcc				42.520(12)	
	21.2	1430	fcc				42.720(21)	
	21.2	1450	fcc				42.854(69)	
3	33.3(2)	300	hcp	19.629(11)	2.4193(6)	3.8725(11)		
	32.7(5)	1030	hcp	20.016(10)	2.4280(5)	3.9206(10)		
	30.6(5)	1190	hcp	20.247(7)	2.4342(4)	3.9456(7)		
	30.2(5)	1240	hcp	20.312(9)	2.4361(5)	3.9521(9)		
	29.3(1.0)	1300**	hcp+fcc	20.411(13)	2.4399(7)	3.9592(13)	41.463(0)	
	29.3(1.1)	1370**	hcp+fcc	20.453(18)	2.4417(9)	3.9611(18)	41.392(0)	
	29.0(6)	1440	hcp+fcc	20.524(14)	2.4434(7)	3.9696(14)	41.285(0)	
	28.4(1)	1470	hcp+fcc	20.559(5)	2.4465(3)	3.9663(3)	41.344(51)	
	28.6(8)	1500	hcp+fcc	20.595(25)	2.4472(14)	3.9710(16)	41.480(37)	
	28.6	1580	fcc				41.652(23)	
	28.6	1620	fcc				41.650(19)	
4	41.0(5)	300	hcp	19.198(26)	2.3956(14)	3.8626(24)		
	43.7(6)	1130	hcp	19.392(13)	2.4019(7)	3.8813(12)		
	43.6(6)	1190	hcp	19.426(13)	2.4028(7)	3.8852(12)		
	43.3(6)	1250	hcp	19.473(10)	2.4043(5)	3.8899(9)		
	42.8(6)	1310	hcp	19.527(9)	2.4060(5)	3.8949(8)		
	42.3(5)	1380	hcp	19.592(7)	2.4081(4)	3.9011(6)		
	41.9(5)	1460	hcp	19.659(7)	2.4103(4)	3.9074(7)		
	41.8(7)	1410	hcp	19.637(14)	2.4106(8)	3.9021(13)		
	41.4(7)	1450	hcp	19.686(13)	2.4125(7)	3.9056(12)		
	41.5(7)	1560	hcp	19.736(13)	2.4139(7)	3.9111(12)		
	41.2(7)	1600	hcp	19.777(17)	2.4157(9)	3.9133(15)		
	41.5(8)	1680	hcp	19.799(25)	2.4158(13)	3.9173(23)		
	41.6(6)	1740	hcp+fcc	19.833(11)	2.4160(6)	3.9234(10)	39.934(0)	
	42.0(8)	1800	hcp+fcc	19.841(24)	2.4161(13)	3.9247(22)	40.055(0)	
	42.1(9)	1870	hcp+fcc	19.868(28)	2.4175(15)	3.9253(26)	40.080(0)	
	42.8(5)	1940	hcp+fcc	19.868(0)	2.4149(0)	3.9338(0)	40.133(10)	
	42.8	2050	fcc				40.204(13)	
	42.8	2090	fcc				40.216(36)	
	42.8	2160	fcc				40.315(44)	
	42.8	2230	fcc				40.344(43)	
	42.8	2260	fcc				40.340(48)	
5	46.0(3)	300	hcp	18.938(15)	2.3856(9)	3.8426(15)		
	50.0(6)	1050	hcp	19.020(12)	2.3882(7)	3.8507(11)		
	50.3(6)	1120	hcp	19.036(10)	2.3885(5)	3.8530(9)		
	50.6(5)	1230	hcp	19.068(7)	2.3890(4)	3.8579(6)		

	50.9(5)	1350	hcp	19.108(4)	2.3897(2)	3.8637(4)	
	52.0(5)	1530	hcp	19.124(5)	2.3901(3)	3.8657(5)	
	52.6(8)	1620	hcp	19.139(17)	2.3904(9)	3.8676(16)	
	52.8(1.3)	1750	hcp	19.186(44)	2.3914(24)	3.8739(41)	
6	75.8(1.2)	300	hcp	17.705(43)	2.3355(25)	3.7481(42)	
	70.1(1.6)	1080	hcp	18.135(48)	2.3563(22)	3.7716(72)	
	70.7(1.5)	1140	hcp	18.133(42)	2.3553(19)	3.7745(62)	
	70.8(1.3)	1200	hcp	18.151(35)	2.3551(16)	3.7789(53)	
	70.5(8)	1300	hcp	18.194(16)	2.3549(7)	3.7886(24)	
	68.7(7)	1460	hcp	18.323(10)	2.3596(5)	3.8000(16)	
	71.0(8)	1510	hcp	18.247(14)	2.3540(6)	3.8025(22)	
	71.0(1.0)	1650	hcp	18.301(21)	2.3552(8)	3.8096(36)	
	70.8(1.0)	1760	hcp	18.347(24)	2.3570(9)	3.8134(42)	
	70.6(1.1)	1840	hcp	18.387(25)	2.3585(9)	3.8169(43)	
	70.6(9)	1910	hcp	18.415(21)	2.3595(8)	3.8193(36)	
	71.2(9)	1960	hcp	18.410(17)	2.3600(8)	3.8169(26)	
	71.0(7)	2020	hcp	18.444(9)	2.3616(4)	3.8187(14)	
Fe-6.5Si (laser heating)							
1	24.0(1.3)	300	hcp	20.321(14)	2.4382(8)	3.9471(14)	
	28.8(2.3)	1320	hcp	20.539(10)	2.4438(5)	3.9713(9)	
	30.5(2.5)	1520	hcp	20.544(10)	2.4440(5)	3.9717(9)	
	29.6(2.4)	1500	hcp	20.602(9)	2.4457(5)	3.9773(8)	
	28.2(2.3)	1360	hcp	20.612(9)	2.4459(5)	3.9784(9)	
	28.0(2.3)	1430	hcp	20.671(9)	2.4473(3)	3.9854(12)	
	29.5(2.8)	1610	hcp	20.683(36)	2.4465(15)	3.9900(51)	
	29.5(3.1)	1640	hcp	20.695(60)	2.4507(25)	3.9788(82)	
	29.5(2.8)	1750	hcp	20.777(29)	2.4513(10)	3.9927(44)	
	29.5	1850	hcp+fcc	-	-	-	42.569(51) one peak for hcp
2	62.1(3.5)	300	hcp	18.308(55)	2.3616(21)	3.7904(93)	
	64.0(3.9)	1480	hcp	18.620(32)	2.3702(10)	3.8271(57)	
	64.0(3.7)	1600	hcp	18.664(20)	2.3702(6)	3.8364(37)	
	63.7(3.6)	1690	hcp	18.717(11)	2.3703(3)	3.8468(19)	
	66.0(5.3)	1930	hcp	18.711(77)	2.3733(8)	3.8360(157)	
	59.5(6.6)	2040	hcp	19.064(158	2.3848(13)	3.8706(318)	
	53.0(3.5)	2140	hcp	19.456(0)	2.3960(0)	3.9134(0)	
	56.6(3.6)	2240	hcp	19.309(0)	2.3859(0)	3.9169(0)	
	56.6(3.6)	2340	fcc	-	-	-	39.548(156)

* The uncertainty in temperature in the resistive and laser heating are typically 50 K and 10%, respectively.

** Temperature uncertainty is as large as ±100 K.

a

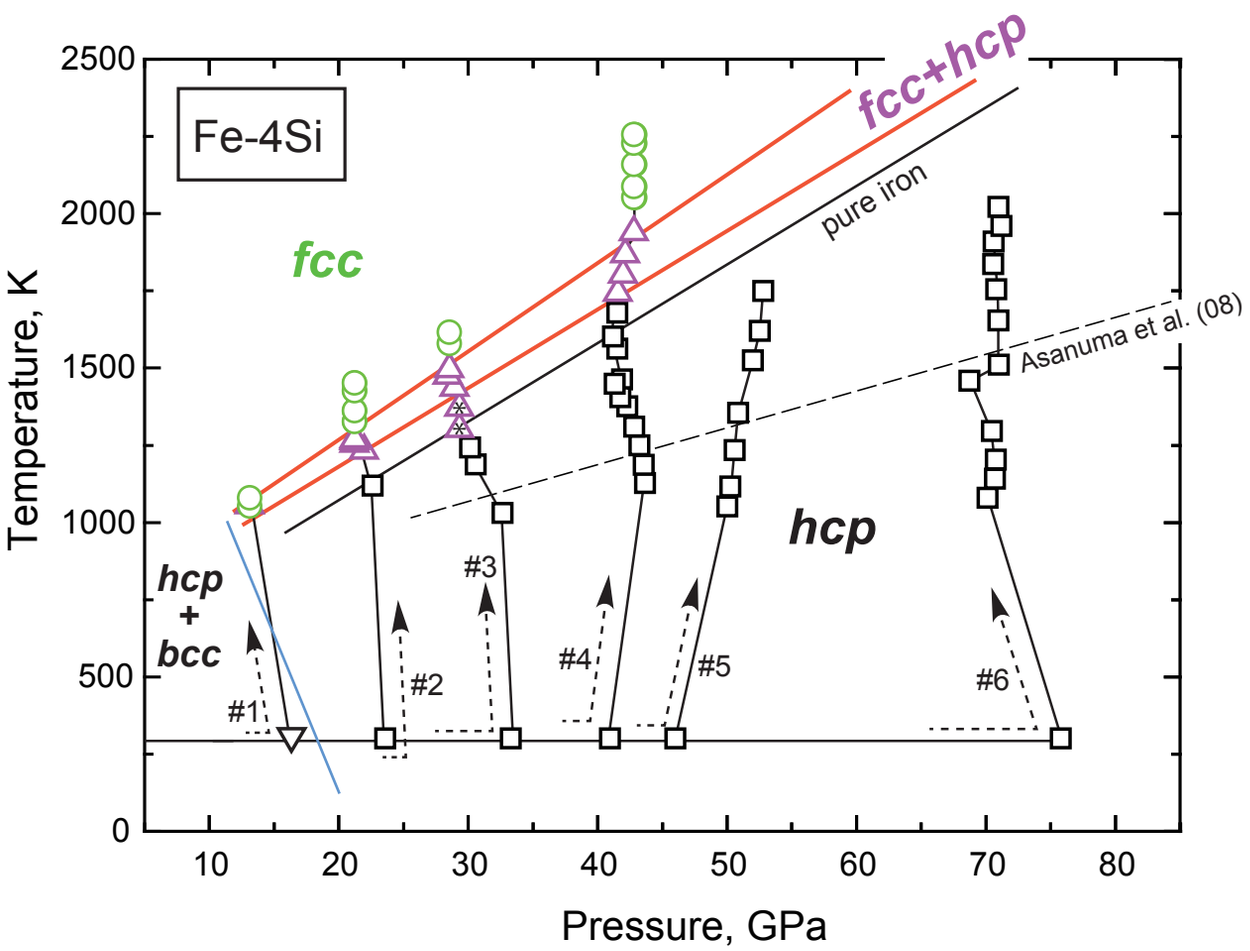
Fe-4Si
fcc
fcc+hcp
pure iron
Asanuma et al. (08)
hcp
hcp
+
bcc
#1
#2
#3
#4
#5
#6
Temperature, K
Pressure, GPa
0
500
1000
1500
2000
2500
10
20
30
40
50
60
70
80

b

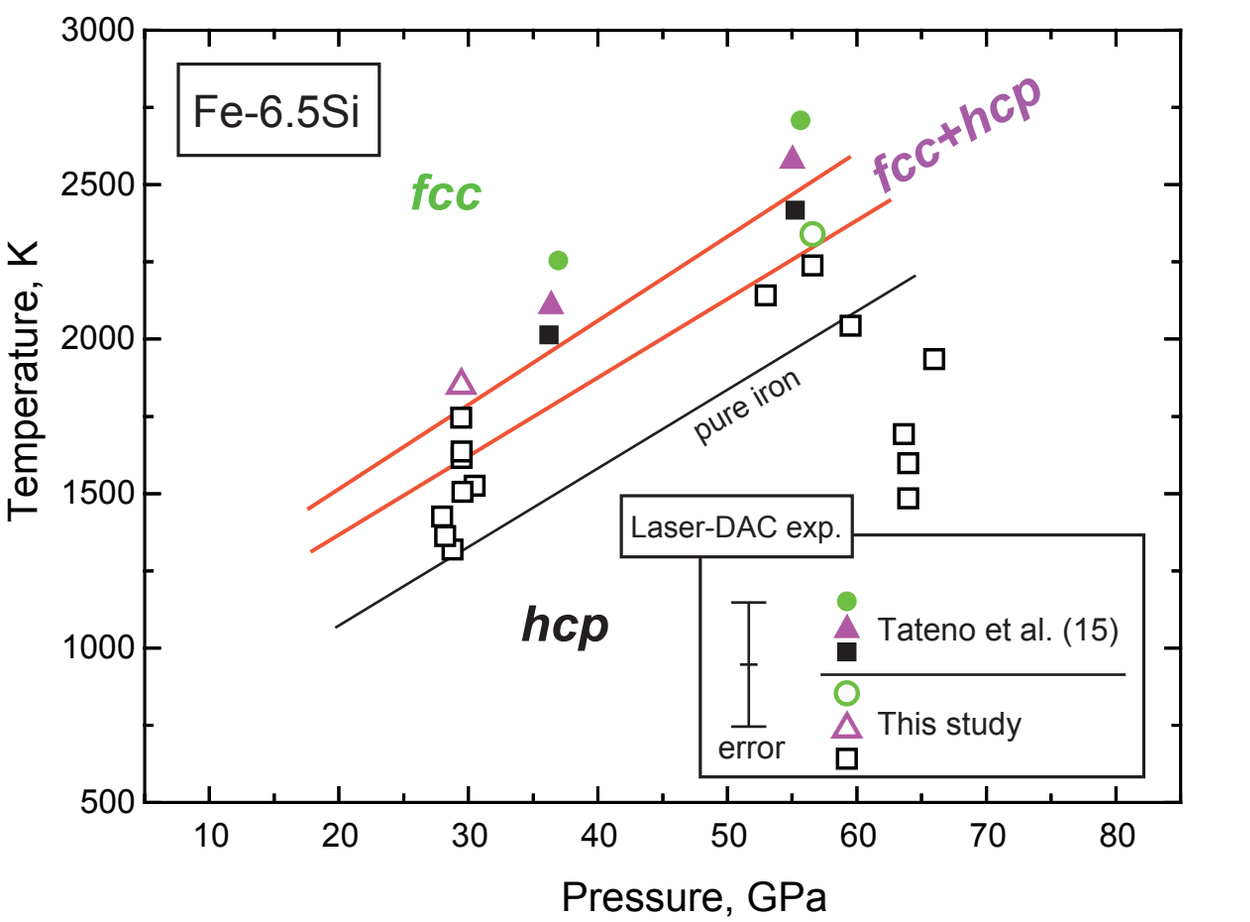
Fe-6.5Si
fcc
fcc+hcp
pure iron
hcp
Laser-DAC exp.
error
Tateno et al. (15)
This study
Temperature, K
Pressure, GPa
500
1000
1500
2000
2500
3000
10
20
30
40
50
60
70
80

figure 1

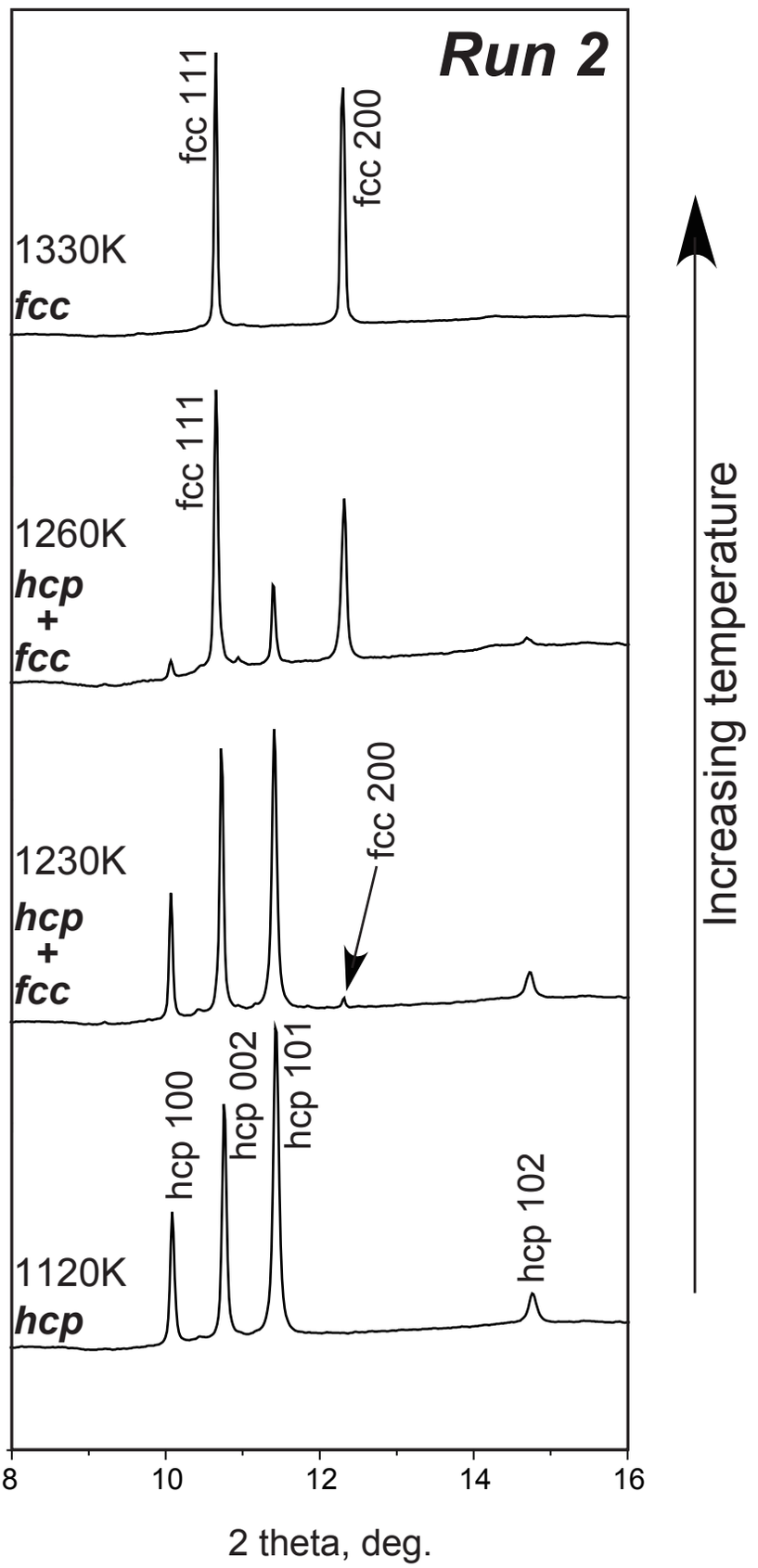
Run 2
fcc 111
fcc 200
1330K
fcc
fcc 111
1260K
hcp
+
fcc
fcc 200
1230K
hcp
+
fcc
hcp 100
hcp 002
hcp 101
hcp 102
1120K
hcp
Increasing temperature
8
10
12
14
16
2 theta, deg.

figure 2

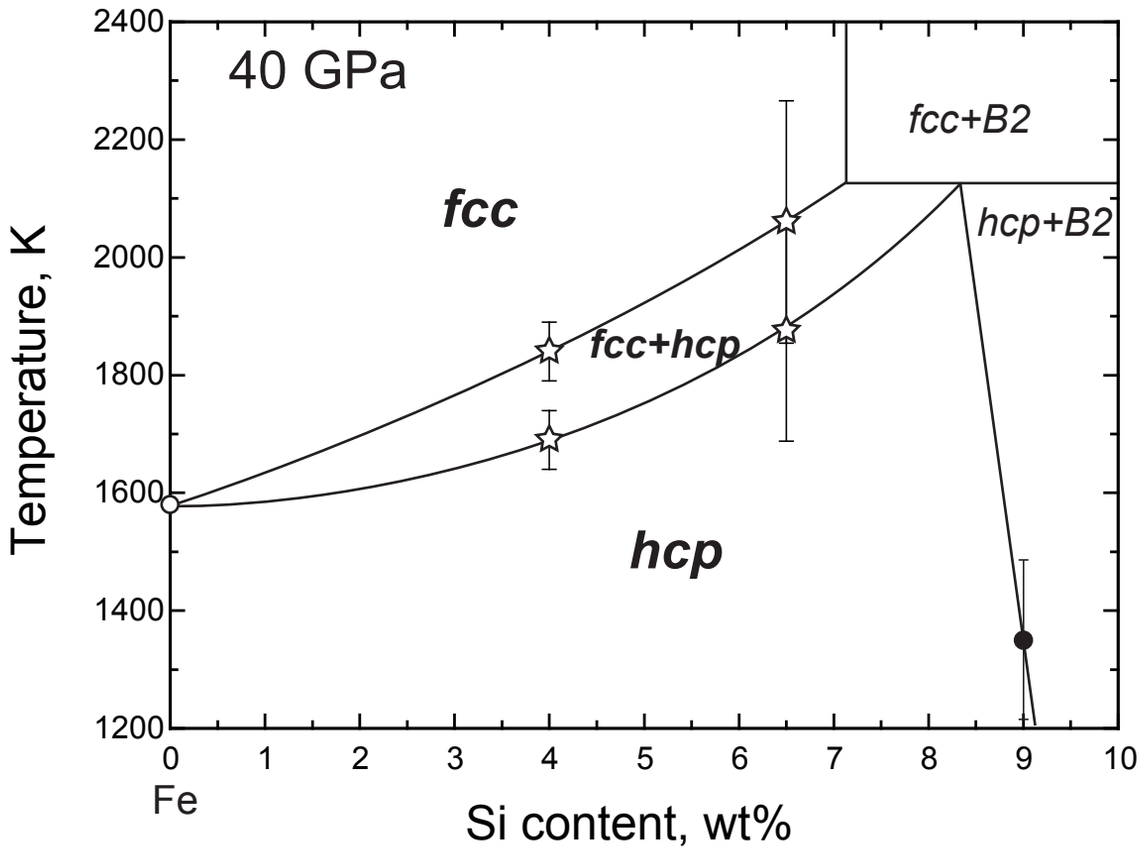
40 GPa
fcc
fcc+B2
hcp+B2
fcc+hcp
hcp
Temperature, K
Si content, wt%
Fe
2400
2200
2000
1800
1600
1400
1200
0
1
2
3
4
5
6
7
8
9
10

figure 3

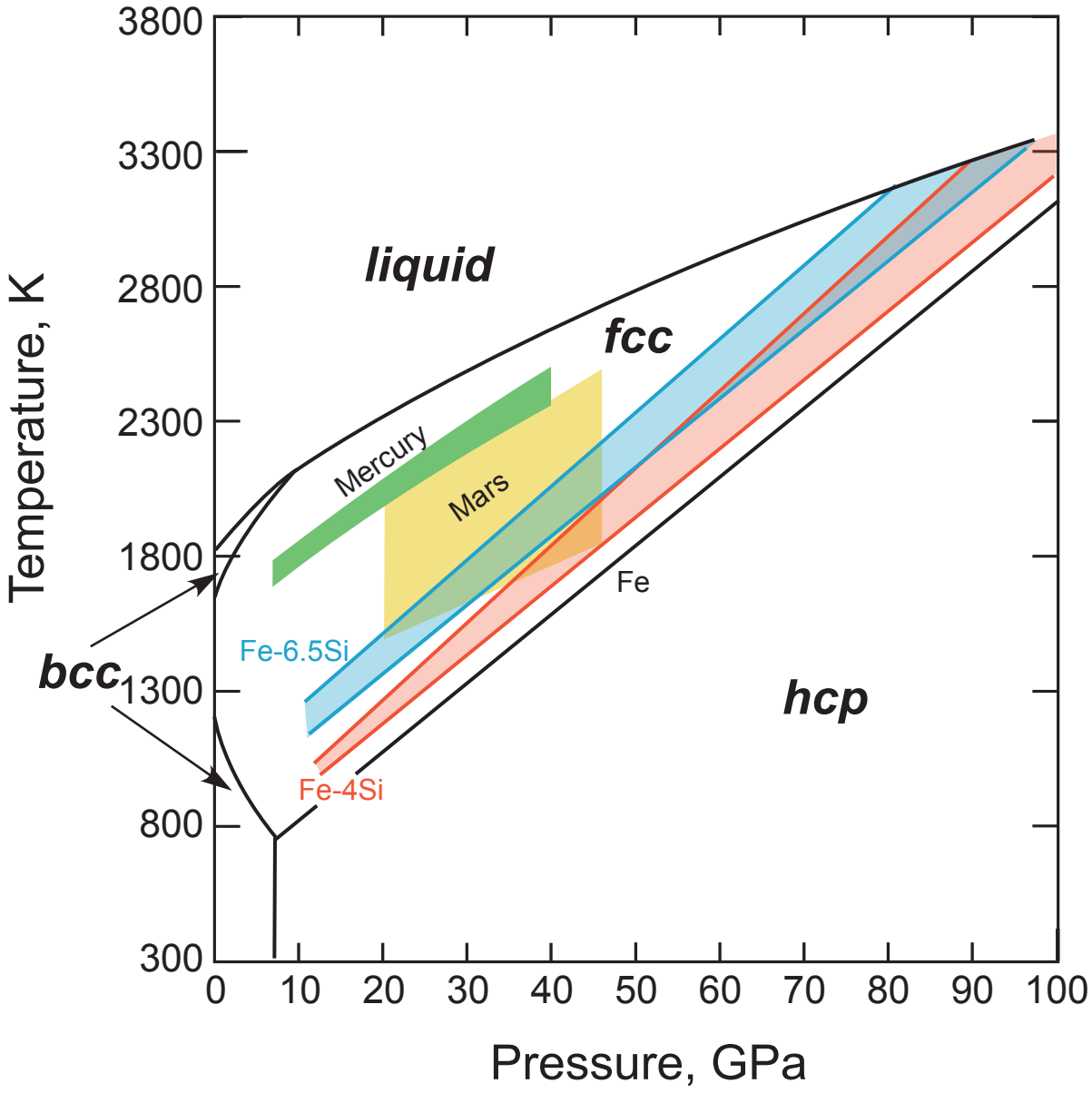
3800
3300
2800
2300
1800
1300
800
300
Temperature, K
0
10
20
30
40
50
60
70
80
90
100
Pressure, GPa
liquid
fcc
hcp
bcc
Mercury
Mars
Fe
Fe-6.5Si
Fe-4Si

figure 4